

Article

Not peer-reviewed version

---

# Design and Optimization of X-Ray Collimators for Preclinical Minibeam Radiation Therapy

---

[Umberto Crimaldi](#), [Nastassja Luongo](#), [Laura A. Cerbone](#), [Roberto Pacelli](#), [Paolo Russo](#)<sup>†</sup>,  
[Giovanni Mettivier](#)<sup>\*,†</sup>

Posted Date: 25 February 2026

doi: 10.20944/preprints202602.1437.v1

Keywords: minibeam radiation therapy; Monte Carlo simulations; TOPAS; X-rays



Preprints.org is a free multidisciplinary platform providing preprint service that is dedicated to making early versions of research outputs permanently available and citable. Preprints posted at Preprints.org appear in Web of Science, Crossref, Google Scholar, Scilit, Europe PMC.

Copyright: This open access article is published under a [Creative Commons CC BY 4.0 license](#), which permit the free download, distribution, and reuse, provided that the author and preprint are cited in any reuse.

Disclaimer/Publisher's Note: The statements, opinions, and data contained in all publications are solely those of the individual author(s) and contributor(s) and not of MDPI and/or the editor(s). MDPI and/or the editor(s) disclaim responsibility for any injury to people or property resulting from any ideas, methods, instructions, or products referred to in the content.

Article

# Design and Optimization of X-Ray Collimators for Preclinical Minibeam Radiation Therapy

Umberto Crimaldi <sup>1,2</sup>, Nastassja Luongo <sup>1,2</sup>, Laura A. Cerbone <sup>2,3,4</sup>, Roberto Pacelli <sup>1,5</sup>, Paolo Russo <sup>2,4,†</sup> and Giovanni Mettivier <sup>2,4,†,\*</sup>

<sup>1</sup> Azienda Ospedaliera Universitaria Policlinico Federico II, I-80131, Napoli, Italy

<sup>2</sup> Istituto Nazionale di Fisica Nucleare, Sezione di Napoli, I-80126, Napoli, Italy

<sup>3</sup> Scuola Superiore Meridionale, I-80134, Napoli, Italy

<sup>4</sup> Dipartimento di Fisica "Ettore Pancini", Università di Napoli Federico II, I-80126, Napoli, Italy

<sup>5</sup> Dipartimento di Scienze Biologiche Avanzate, Università di Napoli Federico II, I-80131, Napoli, Italy

† These authors contributed equally to this work.

\* Correspondence: mettivier@na.infn.it

## Featured Application

This work provides insights into technical details of beam collimator design for a preclinical radiation therapy research technique with arrays of sub-millimeter beamlets of kilovoltage X-rays, a form of spatially fractionated radiation therapy currently investigated for possible translation to the clinical environment.

## Abstract

Spatially fractionated radiotherapy with X-ray minibeam (x-MBRT) aims to increase normal-tissue tolerance by delivering alternating high- and low-dose regions. We provide a Monte Carlo-based framework to design and optimize multislit collimators, quantifying how geometry and material govern peak-valley modulation. A validated digital twin of the SmART X-RAD225Cx irradiator was implemented in TOPAS/Geant4. Various x-MBRT collimators were simulated with parallel or divergent slits. The parameter space covered slit width  $w$  (0.1–0.9 mm), center-to-center spacing  $CTC$  (1–3 mm), thickness  $T$  (1–5 mm), and acceptance angle  $\theta$ . Dose was scored in a  $2 \times 2 \times 2$  cm<sup>3</sup> water phantom at 1 cm depth. The valley dose increased linearly with the filling factor ( $w/CTC$ ) and as  $\sim T^2$ . For fixed  $w/CTC$ ,  $PVDR$  increases with larger  $CTC$  via an increase of peak dose, with valley dose nearly constant. Peak transmission saturated at  $\theta \approx 3^\circ$ , indicating minimal benefit from larger acceptance. Divergent slits yielded flatter lateral profiles but higher valley doses than parallel slits, reducing  $PVDR$  around the central axis. This Monte Carlo study provides insights for optimizing collimator geometries in x-MBRT using small-animal irradiators, informing the design of more effective collimation systems to enhance treatment precision and normal tissue sparing.

**Keywords:** minibeam radiation therapy; Monte Carlo simulations; TOPAS; X-rays

## 1. Introduction

Unconventional radiotherapy approaches (including high and ultra-high dose rate or spatially varying dose delivery) are currently under investigation [1], mainly preclinically, with particular attention to producing improved tolerance of healthy tissues or to determine an improved tumour control. Radiation sources include high-energy (MeV) protons, electrons, or photons, as well as low-energy (keV) photons produced by orthovoltage X-ray tubes. A class of promising strategies, which potentially permits the implementation of this approach, is spatially fractionated radiation therapy (SFRT), in which the radiation dose is delivered purposely in a nonuniform spatial pattern, creating alternating regions of high and low dose values. Various SFRT techniques have been proposed and

are well investigated in the literature, including GRID therapy, lattice therapy, microbeam radiation therapy (MRT), and minibeam radiation therapy (MBRT) [2-4]. Current evidence suggests that MBRT can achieve effective tumour control while significantly reducing normal tissue radiotoxicity [5]. Indeed, over the past decades, extensive preclinical research in animal models has demonstrated that MBRT with kilovoltage photons may provide superior normal tissue sparing and tumour control, compared with conventional homogeneous irradiation fields with broad beams [5]. Spatial dose modulation is typically achieved through incident beam attenuation using a multi-slit collimator positioned in front of the radiation source, which, in a common approach, determines miniplanar beams with beamlets spaced in a one-dimensional array. In typical implementations, MBRT is characterized by arrays of submillimetric beams, typically 0.1–2 mm wide, separated by a fraction of a millimeter to several millimeters [6]; single or few-view irradiations of the target volume are typically utilized in preclinical radiotherapy treatments.

Moreover, beyond the practical advantage of using hospital-based commercial X-ray irradiators rather than large synchrotron radiation facilities as in MRT research, the relatively larger beamlet widths of MBRT treatment (with respect to 0.05-0.10 mm beamlets) also provide increased tolerance to organ and tumour motion during treatment. This feature expands the range of feasible preclinical studies at the hospital level and may ultimately facilitate the clinical translation of the technique.

Previous investigations with kilovoltage X-rays have sought to optimize photon-minibeam energy [7], generally showing that orthovoltage X-rays are preferable to gamma rays due to reduced lateral scattering, which preserves a higher peak-to-valley dose ratio (PVDR). Studies have also emphasized the biological relevance of the valley doses [8, 9] mainly produced by scattered photons within the target volume. Conversely, other reports have shown that higher PVDR values correlate with improved healthy tissue sparing [10, 11]. Preclinical MBRT studies with kilovoltage X-rays (x-MBRT) have been performed using various small-animal irradiation platforms, each employing different beam delivery systems and collimator geometries. In 2024, the first human patients were treated with x-MBRT [12] using an orthovoltage X-ray source, marking a milestone in the translation of this technique to the clinic.

Despite extensive *in silico* collimator design studies [13, 14], there is still no consensus on the “optimal” collimator geometry for achieving the best therapeutic window in x-MBRT. Indeed, the identification of a universally optimal geometry – if such configuration exists – depends on a complex combination of geometrical factors (related to both irradiator and collimator), dosimetric parameters, X-ray beam quality, available power source and dose rate, collimator material, beam divergence, beam field size, distance of the beam from the collimator, as well as the size, shape and position of the target within the animal body. In this context, Monte Carlo (MC) simulations play a significant role in optimizing the dose delivery pattern via virtual dosimetry studies. This approach enables the systematic and independent variation of a reduced set of key irradiation parameters in controlled virtual experiments, through the use of a digital twin of the irradiation source, irradiation setup, and target object (including small-animal computational models).

Following our previous study on a virtual dosimetry platform for preclinical x-MBRT [15], the present study focuses on optimizing the geometric design of x-MBRT collimators for preclinical irradiations with a commercial system. MC simulations are employed to investigate the relationship between geometrical parameters of both parallel and diverging collimators and key dose parameters in the irradiation session.

A specific investigative goal is to show, computationally, the difference of three-dimensional (3D) dose distributions within the target, using an x-MBRT collimator, compared with an open beam irradiation, having the same field size. This strategy isolates the dosimetric effect of the MBRT collimator itself, independently of the irradiation geometry (i.e., distances and field size), which remains common to a corresponding conventional broad-beam irradiation, while systematically varying the collimator design parameters.

Such an approach closely reflects typical preclinical MBRT studies, where treatment outcomes in tumor-bearing small animals irradiated with minibeamlets are compared with cohorts of animals receiving either equivalent open-beam irradiation (without an MBRT collimator) or no irradiation.

In this framework, a direct one-to-one comparison of 3D dose distributions (MBRT vs. open beam) via virtual dosimetry would be beneficial for analyzing treatment outcomes and estimating the x-MBRT dose needed to deliver the same target dose as in the corresponding open-beam treatment. A further advantage of this approach is the possibility of incorporating into the MC-based dosimetry plan a digital twin of the tumor-bearing animal, derived from a computed tomography scan of the animal, performed pre-treatment on the same irradiation platform if equipped with a built-in imaging unit. Finally, this study represents a basic step in our efforts for devising a preclinical x-MBRT treatment planning system based on MC simulations, for which we are also implementing GPU-based MC simulation tools (called VIT-MBRT platform) for fast and validated virtual imaging and dosimetry studies with kilovoltage X-rays [15,16].

## 2. Materials and Methods

### 2.1. Setup Description

The simulated setup was based on the small animal irradiator X-RAD225Cx SmART (Precision X-Ray Irradiation, North Branford, CT, USA) available at the Preclinical Imaging Facility of the San Raffaele Scientific Institute, Milan, Italy. The X-RAD system employs an orthovoltage X-ray tube equipped with a tungsten anode with dual focal-spot sizes (5 mm for treatment and 0.3 mm for imaging), mounted on a rotational C-arm gantry for image-guided preclinical irradiation. For this irradiator, we devised a digital twin (Figure 1) implemented in the MC simulation code, validated in previous work [17]. The beam went through two lead pre-collimators and an MBRT collimator. The simulated geometry is reported in Figure 1. The pre-collimators were two  $7.1 \times 7.1 \times 0.6$  cm<sup>3</sup> lead collimators positioned at 9.8 cm and at 23.2 cm from the source, and with an aperture of  $1.44 \times 1.44$  cm<sup>2</sup> respectively, reducing the beam divergence to 6°. The beam field size at the back side of the collimator face was  $1.44 \times 1.44$  cm<sup>2</sup>. The MBRT collimator was put at 23.3 cm from the focal spot. The description of this collimator is reported in section 2.4.

The tube was operated at 225 kVp and 13 mA, with 2 mm Be inherent filtration and 0.3 mm Cu additional filter. The corresponding X-ray spectrum for the MC simulations was estimated using SpekCalc [18], based on the specific characteristic of the X-RAD SmART X-ray tube [19]. For the irradiator at San Raffaele Hospital, we measured the focal spot size for treatment mode ( $3.5 \times 3.2$  mm<sup>2</sup> FWHM) and the Half Value Layer (HVL) (0.91 mm Cu). A square focal spot with a side of 3.5 mm was used in the simulation.

The simulated target was a water cube phantom ( $2 \times 2 \times 2$  cm<sup>3</sup>) at 25.7 cm from the focal spot of the X-ray tube.

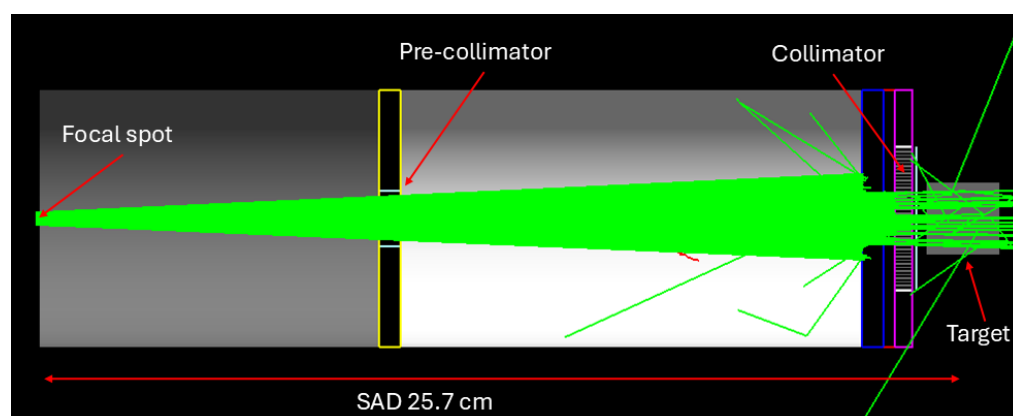


**Figure 1.** The Monte Carlo simulations were performed in TOPAS, with the geometry shown, using custom-designed MBRT collimators that fit within the  $15 \times 15$  mm<sup>2</sup> field collimator of the X-ray irradiator. Dose distribution was scored in a digital  $2 \times 2 \times 2$  cm<sup>3</sup> water phantom with  $0.1 \times 0.1 \times 0.1$  mm<sup>3</sup> voxels; the source-to-object distance was 25.7 cm.

### 2.2. Simulation Setup

MC simulations were performed using TOPAS (Tool for particle simulation) version 3.9, an extension of Geant4 toolbox version 10.5.p01, designed for applications in medical physics, biology and clinical pre-research [20]. The physics list was built with the Geant4\_Modular option using modules recommended for kilovoltage radiotherapy applications (g4em-standard\_opt4", "g4h-phy\_QGSP\_BIC\_HP", "g4decay", "g4ion-binarycascade", "g4h-elastic\_HP", "g4stopping"). For each simulation,  $2 \times 10^{10}$  primary photons were launched to achieve a statistical uncertainty below 2%. Similar simulation approaches have been successfully employed for collimator optimization in spatially fractionated X-ray setups, confirming the reliability of Geant4-based microdosimetric modelling [13, 17].

### 2.3. Evaluated Parameters

The collimator parameters investigated in the MC simulations included both material and geometrical characteristics (Figure 2): center-to-center (CTC) spacing, thickness ( $T$ ), slit width ( $w$ ), width to center-to-center spacing ratio ( $w/CTC$ ), central acceptance angle ( $\theta$ ), as defined by:

$$\theta = \tan^{-1}\left(\frac{\text{width}}{2 \text{ thickness}}\right) \quad (1)$$

The metrics extracted were the *mean dose*, *valley dose*, and *peak-to-valley dose ratio (PVDR)*, commonly used to characterize x-MBRT beam quality [6]. Peak and valley doses were calculated by averaging over the three central peaks or valleys, respectively, while the mean dose was obtained by averaging over the full beam size at 1 cm depth in the target. All values were calculated at 1 cm depth within the water phantom. When comparing the (three-dimensional, 3D) dose distributions produced by x-MBRT irradiations (i.e., with the MBRT collimator in the beam path) in the water phantom, with those produced by the same irradiations without the x-MBRT collimator, with the same  $x$ - $y$  entrance field size (i.e., open beam irradiation), we calculated the MBRT/open beam ratio map,  $R(x, y, z)$ , of the 3D absorbed dose map (in Gy),  $D_{MBRT}(x, y, z)$ , obtained with the MBRT collimator, to the 3D dose map (in Gy) obtained without the collimator,  $D_{open}(x, y, z)$  (with  $z$  the depth in the phantom):

$$R(x, y, z) = \frac{D_{MBRT}(x, y, z)}{D_{open}(x, y, z)}. \quad (2)$$

Hence, we calculated the relative dose as the ratio of (MBRT dose)/(Open beam dose) for fixed X-ray field size, X-ray spectrum, and target-to-collimator distance. Calculated relative dose values for x-MBRT irradiations were then always less than unity (i.e.,  $D_{MBRT}/D_{open} < 1$ ), due to the attenuation of the primary (divergent) X-ray beam produced by the collimator blades. In this way, using such relative dose values, we highlighted the dependence of x-MBRT dose distributions on the specific features of the collimator under investigation, cancelling the influence of parameters which were common to MBRT and open beam irradiations.

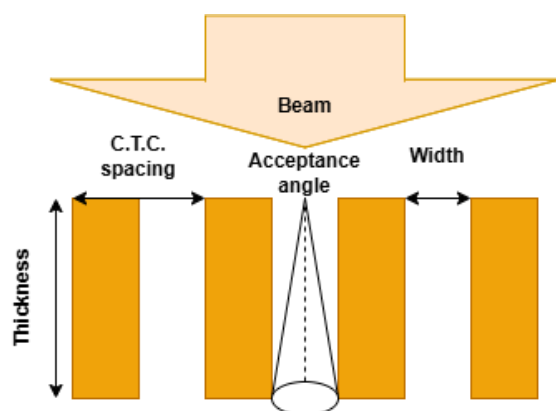


**Figure 2.** Schematic representation of the minibeam geometry in x-MBRT. The primary beam is fractionated into narrow sub-beams by a multi-slit collimator characterized by width, center-to-center (CTC) distance and thickness ( $T$ ).

### 2.4. MBRT Collimator Setup

#### 2.4.1. Parallel MBRT Collimator

An initial series of simulations was performed using lead and tungsten collimators with parallel slits (Figure 3), to compare their attenuation properties under simplified geometries. These collimators were modelled with a fixed thickness ( $T = 5$  mm) and a  $CTC = 1$  mm, while the ratio  $w/CTC$  was varied from 10% to 50% in 10% increments. This configuration enabled the evaluation of the beam opening effects on dose modulation and  $PVDR$ . Subsequently, a more comprehensive analysis was performed on tungsten-based MBRT parallel-slit collimators, exploring a wider range of geometrical configurations, in alignment with literature values [6]. Specifically,  $T$  was varied from 1 mm to 5 mm in 1 mm steps,  $w/CTC$  ranged from 10% to 50%, and the  $CTC$  tested values were 1.0, 1.5, 2.0, and 3.0 mm. In the resulting 3D dose maps evaluated in the water cube, the  $PVDR$ , *valley dose*, and *mean dose* were extracted along lateral dose profiles at 1 cm depth and used as quantitative performance metrics for comparison. This systematic study allowed assessment of how slit width, spacing, and thickness affect the lateral dose distribution in MBRT. The field size was  $1.5 \times 1.5$  cm<sup>2</sup> at the entrance of the water phantom.

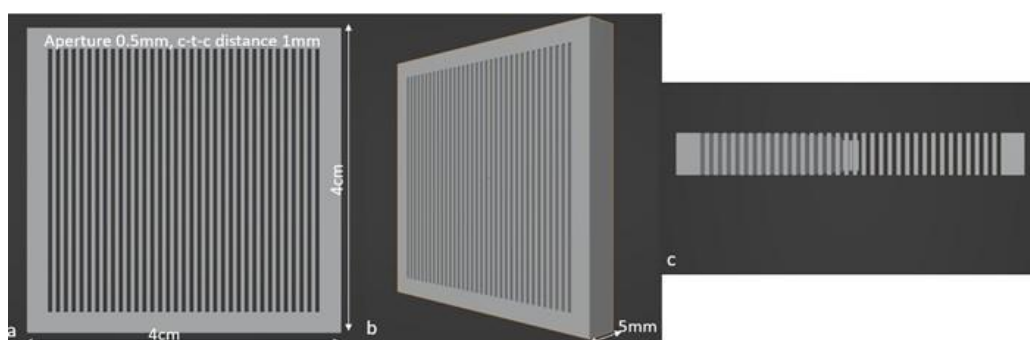


**Figure 3.** Geometry of a parallel collimator: (a) front view, (b) 45° view, and (c) transversal section.

#### 2.4.2. Divergent MBRT Collimator

In addition to the parallel geometries, divergent slit tungsten collimators were analysed (Figure 4). These configurations maintained a constant  $T = 5$  mm and  $CTC = 1$  mm, while varying the  $w/CTC$  ratio from 10% to 50%.

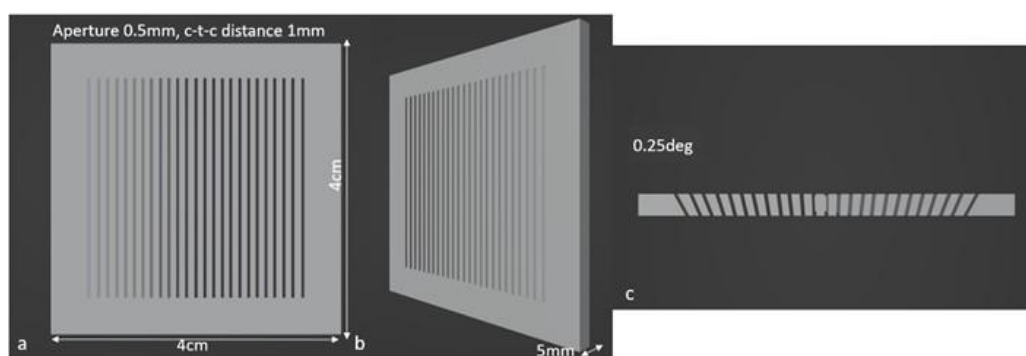


**Figure 4.** Geometry of a divergent collimator: (a) front view, (b) 45° view, and (c) transversal section.

## 3. Results

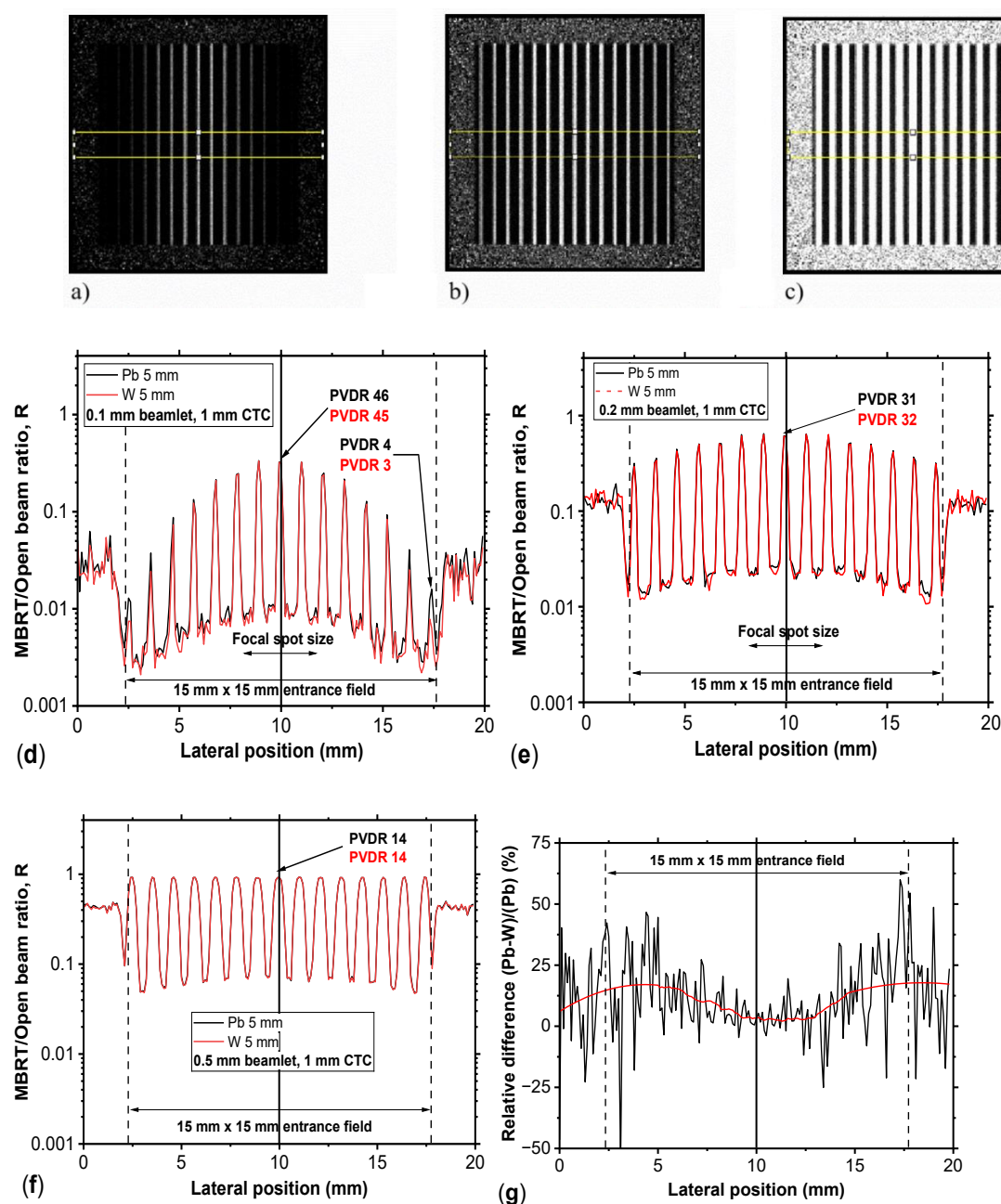
### 3.1. Influence of Collimator Material

We evaluated the absorbed dose MBRT/open beam ratio maps  $R(x,y,z)$  obtained using lead or tungsten MBRT collimators having identical geometrical configurations. Figures 5(a–c) show the  $R(x,y,z)$  distributions in the water phantom at 1 cm depth, obtained using parallel MBRT collimators made of lead and tungsten. Figures 5(d–f) present the corresponding lateral profiles of  $R(x,y,z)$  distributions for collimators with  $T = 5$  mm,  $CTC = 1$  mm, and  $w/CTC$  ratios of 10%, 20%, and 50%, respectively. Both materials exhibit characteristic parabolic-shaped profiles in the peaks and valleys regions, due to beam divergence and lateral scattering, which lead to  $PVDR$  degradation away from the central axis.

Figures 5(g-i) report the percentage dose difference between  $R(x,y,z)$  profiles in Figures 5(d-f) obtained with lead and tungsten collimators, showing the largest deviations for MBRT collimators with smaller apertures. In these cases, the difference profiles display a concave pattern, with minimal variation at the center and maximum lateral discrepancies of approximately 25%, 13%, and 3% for 10%, 20%, and 50%  $w/CTC$  ratios, respectively.

### 3.2. Influence of Collimator's Geometrical Parameters

We analyzed the effect of geometric parameters (specifically, collimator thickness  $T$  and  $w/CTC$  ratio) on the  $R(x,y,z)$  distribution, using tungsten parallel collimators. Figure 6a shows the  $R(x,y,z)$  profiles measured at 1 cm depth in water for  $T = 5$  mm,  $CTC = 1$  mm, and a  $w/CTC$  ratio of 20%, 30% and 50% ( $w = 0.2$  mm, 0.3 mm and 0.5 mm, respectively). As illustrated in Figure 6b, the *valley dose* increases linearly with the  $w/CTC$  ratio, a trend consistent across different  $CTC$  values. This confirms that the  $w/CTC$  ratio, rather than the absolute slit width, influences the *valley dose* and consequently the *PVDR*. Figure 6c shows dose profiles for  $CTC = 1$  mm and  $w/CTC = 30\%$ , while the collimator thickness  $T$  is 1 mm, 3 mm, and 5 mm. In this case, the *valley dose* decreases progressively with increasing thickness  $T$ , following an approximately inverse-quadratic trend (Figure 6d).



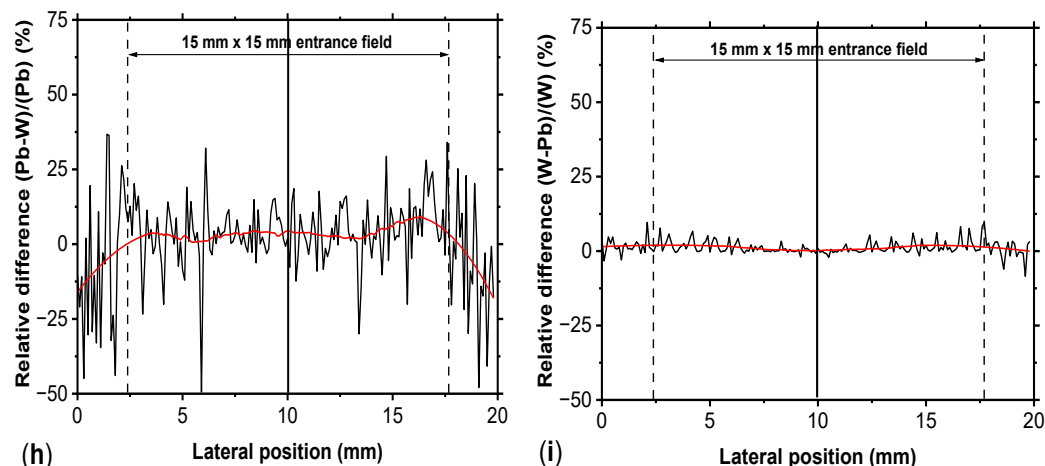


**Figure 5.** Example of the  $R(x,y,z)$  distribution (at 1 cm depth in water,  $15 \times 15 \text{ mm}^2$  field size at the entrance surface of the water phantom) produced by a tungsten parallel MBRT collimators, 5-mm-thick, 1 mm CTC. Beamlet width: (a) 0.1 mm, (b) 0.2 mm, (c) 0.5 mm. The profiles obtained with similar MBRT collimators, but different materials (tungsten, red line, and lead, black line) are shown in panels (d-f). In (g-i) are reported the relative difference between the profile in (d-f).

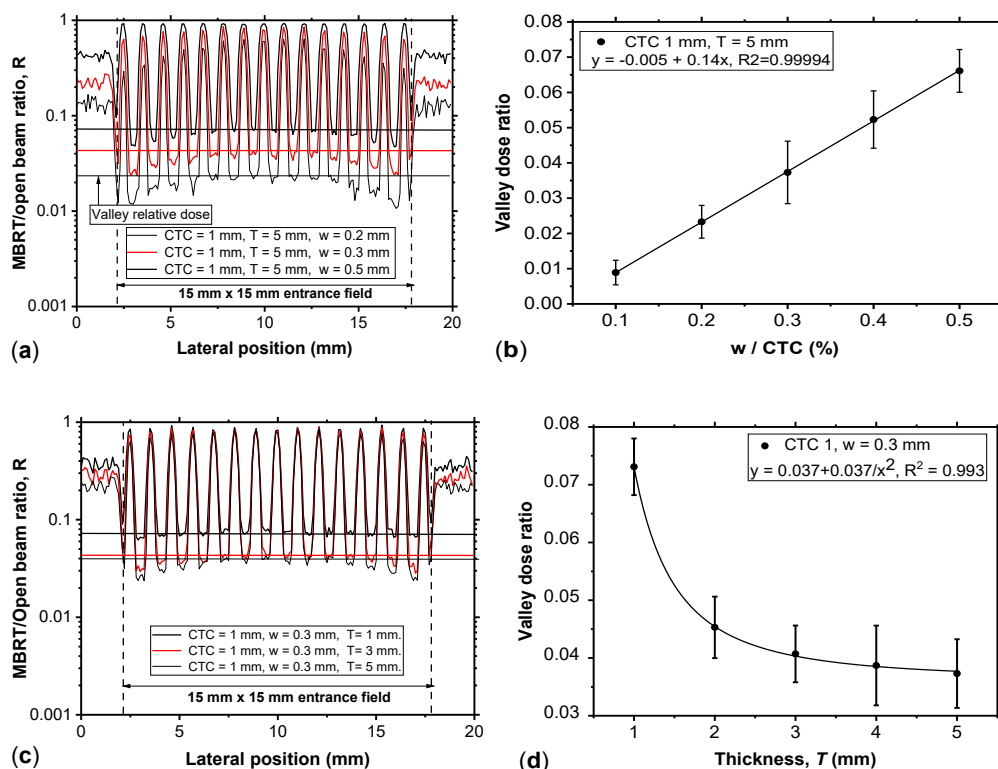


**Figure 6.** (a) Comparison of profiles of the  $R(x,y,z)$  distribution (at 1 cm depth in water,  $15 \times 15 \text{ mm}^2$  field size at the entrance surface of the water phantom) produced by a tungsten MBRT collimators with collimator thickness of 5 mm, CTC of 1 mm and  $w$  of 0.2 mm, 0.3 mm and 0.5 mm. (b) Valley dose ratio as a function of the  $w/\text{CTC}$  ratio. (c) Comparison of profiles of the  $R(x,y,z)$  distribution (at 1 cm depth in water,  $15 \times 15 \text{ mm}^2$  field size at the entrance surface of the water phantom) produced by a tungsten MBRT collimators with collimator thickness of 1 mm, 3 mm and 5 mm,  $w = 0.3 \text{ mm}$  and the CTC distance of 1 mm. (d) Valley dose ratio as a function of thickness  $T$ . An inverse-square law trend was fitted to the data points.

Figure 7a compares the profiles of MBRT/open beam ratio  $R$  from collimators with the same nominal aperture ( $w = 0.3 \text{ mm}$ ) and thickness  $T = 5 \text{ mm}$ , but different CTC distances. The results confirm that the valley dose ratio (evaluated at the level of the three central peaks) depends primarily on the  $w/\text{CTC}$  ratio, rather than on the absolute aperture slit width.

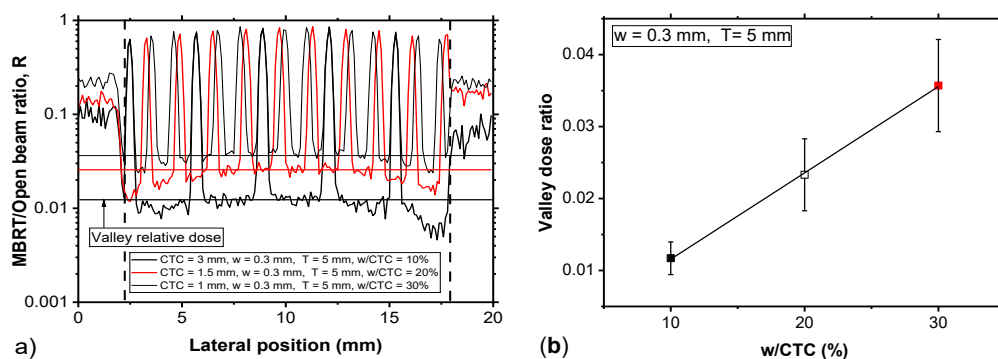


**Figure 7.** a) Profiles of the MBRT/open beam ratio produced by a parallel tungsten MBRT collimators (at 1 cm depth in water,  $15 \times 15$  mm<sup>2</sup> field size at the entrance surface of the water phantom) for slit widths of 0.3 mm, thickness of 5 mm and CTC of 3 mm (thick black line), 1.5 mm (thick red line) and 1 mm (fine black line); b) Valley dose ratio as a function of  $w/CTC$ .

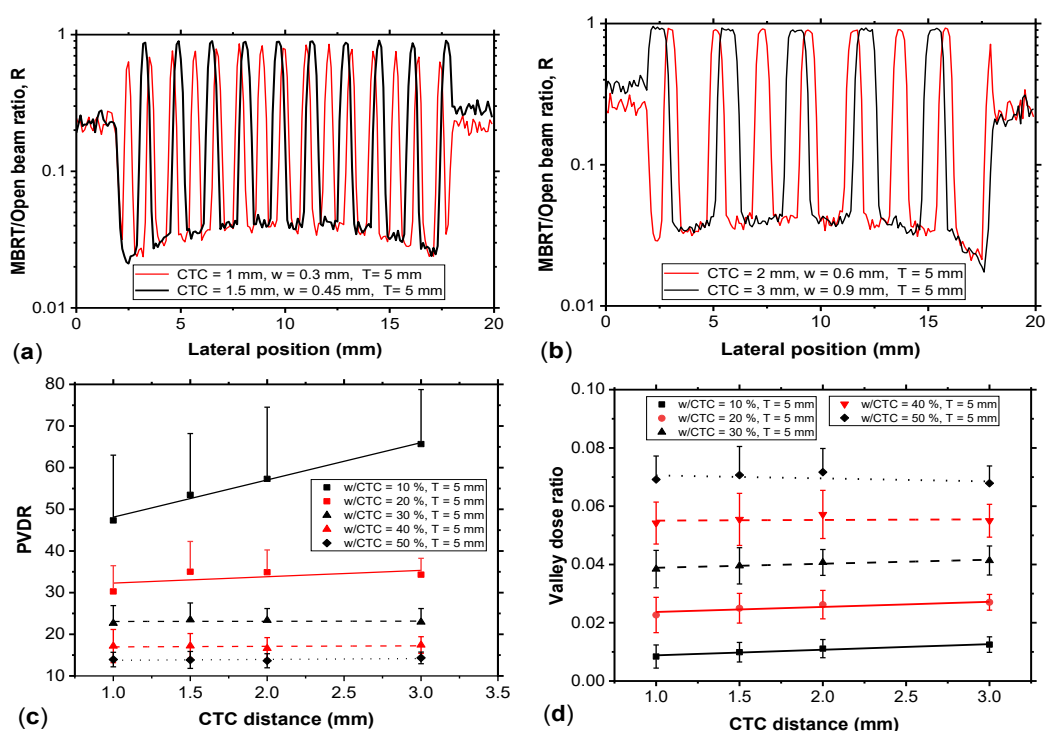


**Figure 8.** (a) Profiles of the MBRT/open beam ratio produced by a parallel tungsten MBRT collimators (at 1 cm depth in water,  $15 \times 15$  mm<sup>2</sup> field size at the entrance surface of the water phantom) for a thickness of 5 mm and CTC of 1 mm and slit width of 0.3 mm (red line) and CTC of 1.5 mm and slit width of 0.45 mm (black line); (b) with a CTC of 2 mm and slit width of 0.6 mm (red line) and CTC of 3 mm and slit width of 0.9 mm (black line); (c) PVDR as a function of CTC distance for several  $w/CTC$  ratios; (d) Valley dose as a function of CTC distance for several  $w/CTC$  ratios.

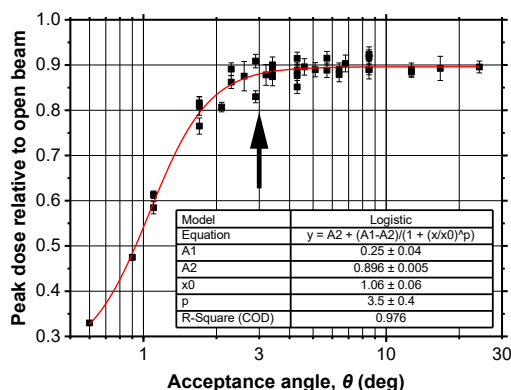


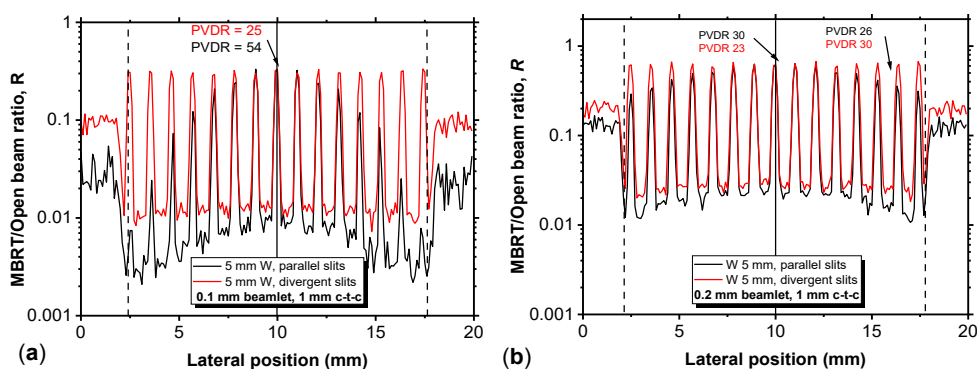
**Figure 9.** Calculated data for relative *peak dose* as a function of collimator acceptance angle (please note the horizontal log scale). A logistic fit is shown. The *peak dose* for the x-MBRT irradiation (relative to open beam irradiation) reaches a saturation level equal to 0.9 (minibeam dose with respect to open beam irradiation dose) for an acceptance angle of about 3° (black arrow), or higher.

Figures 9(a-b) show the dose profiles for tungsten parallel collimators with varying *CTC* distances, while maintaining collimator thickness  $T = 5$  mm and  $w/CTC$  ratio = 30%. The *valley dose* remains approximately constant with *CTC* variations, whereas *PVDR* increases linearly with *CTC* for smaller apertures, owing to a rise in the peak dose value. For *PVDR* calculations, the peak dose was evaluated as the mean of the highest values of the three central peaks.

Finally, Figure 10 illustrates that the peak-dose increases with the acceptance angle  $\theta$ , until reaching a saturation level of approximately  $Peak\ dose_{sat} = 0.9$  (normalized to the open beam) at  $\theta \approx 3^\circ$ , beyond which no further increase is practically observed.

### 3.3. Influence of Collimator's Divergence

The final part of the analysis investigated the impact of divergent versus parallel collimator geometries on dose distribution. A divergent collimator was defined as one whose slits are aligned with the divergence of the beam. In Figure 10 are compared profiles of MBRT/open beam ratio produced by parallel (black line) and divergent (red line) tungsten MBRT collimators for slit widths of 0.1 mm (Figure 10a), 0.2 mm (Figure 10b) and 0.5 mm (Figure 10c),  $CTC = 1$  mm, and  $T = 5$  mm. Profiles are shown on a logarithmic scale to emphasize differences in low-dose regions. Divergent collimators produce flatter lateral dose profiles, characterized by a reduced intensity fall-off away from the beam's central axis. However, the corresponding *valley doses* are consistently higher compared to parallel collimators, resulting in lower *PVDR* values near the central axis.



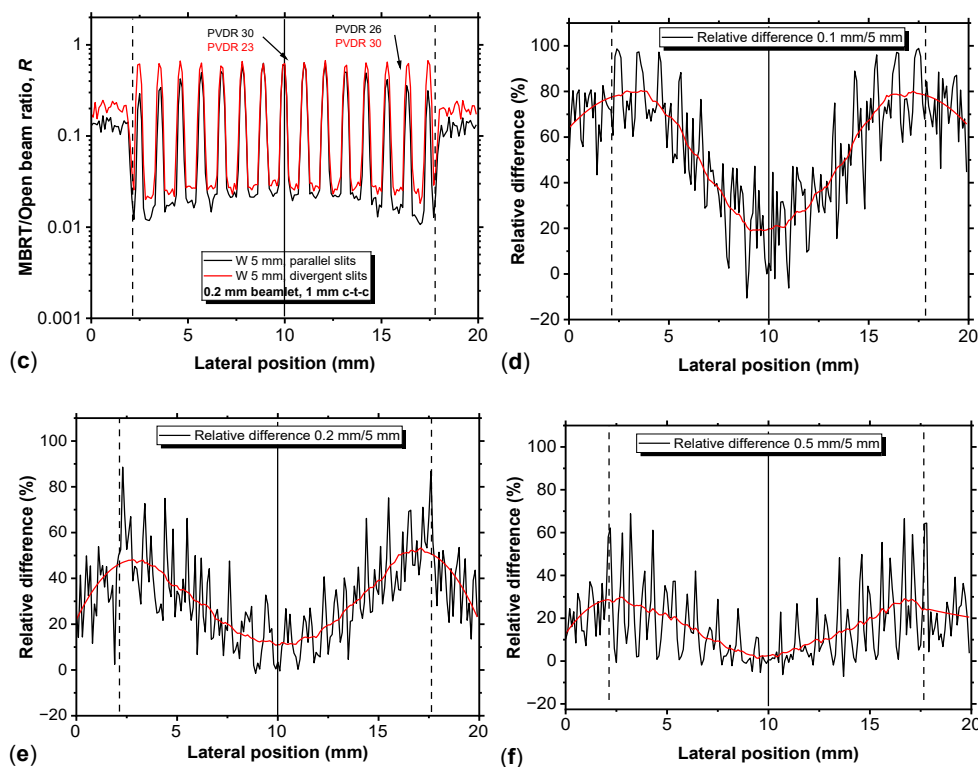


**Figure 10.** Profiles of the MBRT/Open beam ratio produced by parallel (black line) and divergent (red line) tungsten MBRT collimators (at 1 cm depth in water,  $15 \times 15 \text{ mm}^2$  field size at the entrance surface of the water phantom) for slit widths of 0.1 mm (a), 0.2 mm (b) and 0.5 mm (c). In all collimators the collimator thickness is fixed at 5 mm and the distance CTC at 1 mm. Relative differences between the parallel and divergent MBRT collimators profile are reported in d-f.

Figures 11(a–c) summarize these findings:

- Central peak doses are nearly identical for both geometries.
- Valley doses are systematically higher for divergent collimators.
- PVDR values are higher for parallel collimators in the central region, whereas divergent geometries improved lateral uniformity.

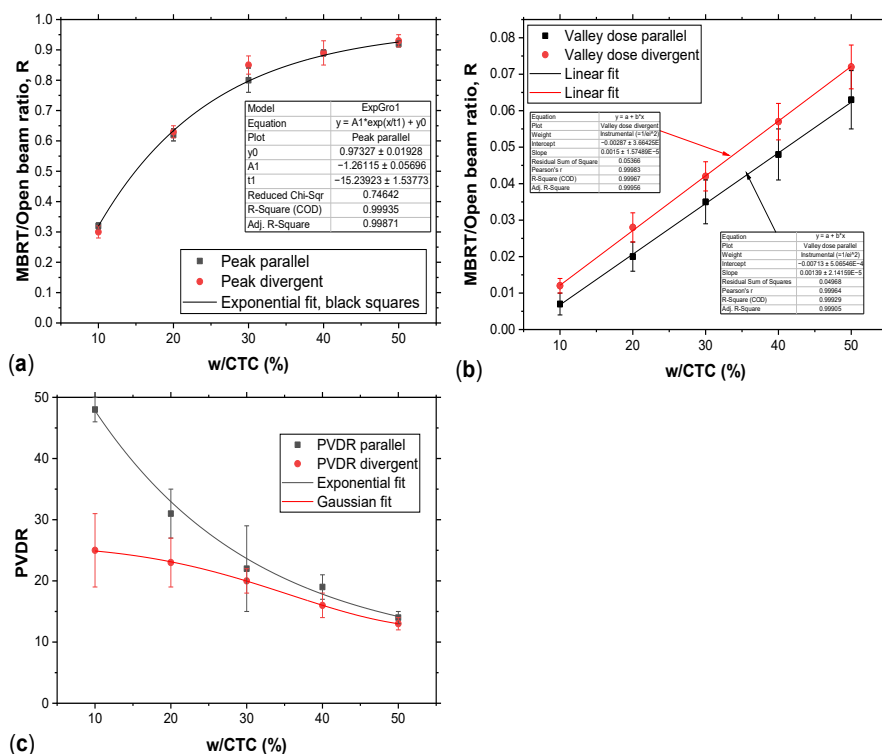


**Figure 11.** (a) Peak dose as a function of the  $w/CTC$  ratio for parallel and diverging collimators. (b) Valley dose curve for parallel and diverging collimators as a function of the  $w/CTC$  ratio. Note that the values for the diverging collimator are always higher than those for the parallel counterpart. (c) Central PVDR curve for parallel and diverging collimators as a function of the  $w/CTC$  ratio. Fits have been shown to follow the data trends.

## 4. Discussion

The present work provides a systematic Monte Carlo–based analysis of how individual geometric parameters of multi-slit collimators influence the fundamental dosimetric descriptors of X-ray minibeam radiation therapy. While several studies have explored collimator fabrication strategies or reported empirical performance metrics [13, 14, 21], a quantitative mapping between geometric design variables and beam-quality indicators such as PVDR, valley dose, and mean dose has remained largely unexplored. The results presented here fill this gap by establishing explicit functional dependencies that can guide rational collimator optimization for preclinical x-MBRT.

The comparison between lead and tungsten collimators (Figure 5) demonstrates that, for thicknesses on the order of 5 mm, both materials yield nearly indistinguishable central-axis PVDR values. This is consistent with the high attenuation coefficients of both materials in the orthovoltage range, where photoelectric absorption dominates. The different profile shapes (Figure 5d–f) due to the parallel collimator geometry and not to collimator material, show a lateral reduction of the peak intensity from 25% to 2% for the smallest ( $w/CTC = 10\%$ , Figure 5g) and greater ( $w/CTC = 50\%$ , Figure 5i) apertures, respectively. This arises from the differential attenuation of the oblique photons' beam, which becomes increasingly relevant at off-axis positions. These results suggest that the choice of collimator material, in the case of a 5-mm-thick MBRT collimator is related only on practical considerations, such as cost, machinability, achievable tolerances, and mechanical stability.

A central outcome of this study is the demonstration that the valley dose exhibits a linear dependence on the  $w/CTC$  ratio (Figure 6b), confirming that the geometric filling factor governs the fraction of scattered photons reaching the inter-beam regions. This observation is consistent with theoretical models of spatially fractionated beams, where valley dose is dominated by low-energy scattered photons whose fluence scales with the open fraction of the collimator [6]. Conversely, the inverse-square dependence of valley dose on collimator thickness ( $D \propto 1/T^2$ ) (Figure 6d) reflects the suppression of lateral photon transport within the slit channel, in agreement with previous Geant4-based analyses of microbeam and minibeam collimators [14, 17]. These relationships provide

a compact parametric framework for predicting valley-dose behaviour without requiring full MC simulations for each geometry.

Thicker collimators more effectively suppress laterally scattered photons within the slits, thereby increasing *PVDR*. However, beyond approximately 4 mm (for tungsten), additional thickness yields diminishing returns while unnecessarily reducing beam transmission and increasing manufacturing complexity and costs—particularly for tungsten.

The acceptance angle  $\theta$  emerges as another critical determinant of peak-dose transmission. As shown in Figure 9, the peak dose increases with  $\theta$  until reaching a saturation plateau at approximately 0.9 (normalized to open beam) for  $\theta \gtrsim 3^\circ$ . This behaviour reflects the interplay between the intrinsic beam divergence of the X-RAD225Cx source and the angular acceptance of the slit channel. When  $\theta$  is smaller than the beam divergence, a portion of the primary fluence is intercepted by the collimator walls, reducing the peak intensity. Once  $\theta$  matches or exceeds the beam divergence, further increases do not enhance transmission. Similar saturation effects have been reported in synchrotron-based MRT studies, where matching the collimator acceptance to the source divergence is essential to preserve peak integrity [5, 6].

The dependence of *PVDR* on *CTC* spacing (Figures 7, 8) further clarifies the geometric trade-offs inherent to MBRT design. For fixed  $w/CTC$  ratios, increasing *CTC* enhances *PVDR* primarily through an increase in *peak dose*, while *valley dose* remains approximately constant. This is consistent with the reduced overlap of lateral scatter tails from adjacent beamlets at larger separations, a phenomenon also observed in proton and electron minibeam configurations [2–4]. However, excessively large *CTC* values reduce the spatial frequency of the minibeam pattern, potentially diminishing the biological benefits associated with spatial fractionation [5, 10]. Thus, the optimal *CTC* must balance dosimetric modulation with biological efficacy.

From these findings, empirical relationships can be derived to guide collimator's design optimization:

$$D_{valley} \propto w/CTC \quad (3)$$

$$D_{valley} \propto \frac{1}{r^2} \quad (4)$$

$$D_{peak}(\theta) \approx 0.9, \text{ for } \theta \geq 3^\circ \quad (5)$$

$$PVDR(\theta) \propto \frac{CTC}{w}, \text{ for } \theta \geq 3^\circ \quad (6)$$

$$PVDR(\theta) \propto T^2, \text{ for } \theta \geq 3^\circ \quad (7)$$

The comparison between parallel and divergent collimators (Figures 10,11) further clarifies the trade-offs between geometric configurations. When slit width, thickness, and spacing are matched, both geometries yield similar central peak doses (Figure 11a). However, divergent collimators produce flatter lateral profiles (Figures 10a–c), improving field uniformity but increasing *valley dose* due to enhanced transmission of scattered photons. These findings are consistent with prior MRT studies showing that divergent geometries increase the contribution of scattered photons to the valley region due to improved alignment between the slit channel and the beam divergence [6]. As a result, *PVDR* is consistently higher for parallel collimators (Figure 11c), making them more suitable for applications where strong spatial modulation and normal-tissue sparing are prioritized. Nevertheless, beams exhibiting strong lateral inhomogeneities could be advantageous during the planning phase, similarly to the use of flattening filter-free (FFF) beams, which have been shown to improve dose delivery efficiency and treatment conformity [20]. Divergent geometries may instead be advantageous for larger irradiation fields where uniformity is desired, although they inherently constrain the focus-to-target distance, reducing flexibility in experimental setups.

Overall, the present results suggest that intermediate geometries (i.e., collimator thicknesses of 2–4 mm and  $w/CTC$  ratios of 20–40%) offer a favourable compromise between *PVDR*, transmission efficiency, and manufacturability. These findings are consistent with the parameter ranges adopted in successful preclinical x-MBRT studies [5, 7, 12]. Importantly, the relationships derived here provide a basis for future treatment-planning strategies, including integration into GPU-accelerated MC platforms such as VIT-MBRT [15,16], enabling rapid optimization of collimator designs tailored to specific biological endpoints, beam qualities, and anatomical targets.

Future work will include experimental validation of the MC estimated dose maps using radiochromic film dosimetry and micro-ionization chambers, as well as preclinical *in vivo* studies to

assess the predictive accuracy of the simulation-derived *PVDR* and *valley-dose* metrics. Given the increasing interest in clinical translation of x-MBRT [12], establishing robust, physics-based design criteria for collimators is essential for ensuring reproducible and biologically effective dose delivery.

## 5. Conclusions

This study presented a systematic Monte Carlo-based analysis of mini-beam collimator geometries for an MBRT investigation in small animals using a preclinical X-ray irradiator. The simulations of various metal collimators investigated the influence of collimator material, slit width, CTC spacing, thickness, and geometry on the dose to water distribution, in a water phantom representative of small-animal experiments. Expressing the dose maps in relative terms with respect to open beam irradiation permits linking MBRT absorbed dose fields to open field beams, whose dosimetry is already available to the experimenter by the irradiator's preclinical treatment planning system. Results showed that the *valley-dose* was found to increase linearly with the width-to-spacing ratio ( $w/CTC$ ) and to decrease approximately with the inverse square of the collimator thickness, establishing the role of these two parameters as geometric determinants of spatial modulation in x-MBRT. The *peak dose* saturated for acceptance angles around  $3^\circ$ , confirming that collimator divergence should be matched to the beam geometry to minimize unnecessary attenuation or valley overexposure. Parallel geometries preserved higher *PVDR* and stronger spatial modulation, whereas divergent geometries offered smoother lateral profiles, making them more suitable for large irradiation fields. Overall, intermediate configurations, with thickness between 2–4 mm and  $w/CTC$  ratio of 20–40%, emerged as the most balanced design window, combining efficient dose modulation, acceptable transmission, and practical manufacturability. However, the optimal geometry remains application-specific, determined by the intended biological endpoint and specific experimental setup.

**Author Contributions:** Conceptualization, P.R. and G.M.; methodology, P.R.; software, U.C. and N.L.; validation, U.C., N.L., L.A.C., G.M. and P.R.; formal analysis, U.C.; writing—original draft preparation, U.C., P.R.; writing—review and editing, U.C., G.M., N.L., L.A.C., R.P. and P.R.; supervision, G.M., P.R.; project administration, G.M., R.P. All authors have read and agreed to the published version of the manuscript.

**Funding:** This research was funded in the framework of the PNRR project “Sviluppo e ottimizzazione della radioterapia con mini fasci a raggi X” (PNRR-POC-2022-12376062).

**Acknowledgments:** All simulations carried out using the CPU-based and the GPU-accelerated resources of INFN (Istituto Nazionale di Fisica Nucleare), Italy. This work contributes also to the project VITA5 (Virtual Imaging TriAls) funded by INFN. Thanks are due to the authors' colleagues at San Raffaele Scientific Institute (Milan, Italy) for useful discussions and exchange of information within the PNRR MBRT project (leaders: A. Spinelli and C. Fiorino).

**Conflicts of Interest:** The authors declare no conflicts of interest.

## Abbreviations

The following abbreviations are used in this manuscript:

CTC	Center To Center distance
MBRT	Mini Beam Radiation Therapy
MRT	Microbeam Radiation Therapy
PVDR	Peak Valley Dose Ratio
SFRT	Spatially Fractionated Radiation Therapy
VIT	Virtual Imaging Trial

## References

1. Griffin R.J.; Ahmed M.M.; Amendola B.; Belyakov O.; Bentzen S.M.; Butterworth K.T.; Chang S.; Coleman C.N.; Djonov V.; Formenti S.C.; Glatstein E.; Guha C.; Kalnicki S.; Le Q.T.; Loo B.W.; Mahadevan A.; Massacesi M.; Maxim P.G.; Mohiuddin M.; Mohiuddin M.; Mayr N.A.; Obcemea C.; Petersson K.; Regine W.; Roach M.; Romanelli P.; Simone C.B.; Snider J.W.; Spitz D.R.; Vikram B.; Vozenin M.C.; Wahab M.A.;

- Welsh J.; Wu X.; Limoli C.L. Understanding High-Dose, Ultra-High Dose Rate, and Spatially Fractionated Radiation Therapy. *Int. J. Radiat. Oncol. Biol. Phys.* **2020**, 107(4), 766–78. <https://doi.org/10.1016/j.ijrobp.2020.03.028>.
2. Yan W.; Khan M.K.; Wu X.; Simone II C.B.; Fan J.; Gressen E.; Zhang X.; Limoli C.L.; Bahig H.; Tubin S.; Mourad W.F. Spatially fractionated radiation therapy: History, present and the future. *Clin. Transl. Radiat. Oncol.* **2020**, 20, 30–38. <https://doi.org/10.1016/j.ctro.2019.10.004>.
  3. Prezado Y.; Wardak Z.; Serduc R. Spatially fractionated radiotherapy: An emerging treatment paradigm. *Nat. Rev. Clin. Oncol.* **2021**, 18(12), 729–740. <https://doi.org/10.1038/s41571-021-00522-7>.
  4. Prezado Y.; Grams M.; Jouglar E.; Martínez-Rovira I.; Ortiz R.; Seco J.; Chang S. Spatially fractionated radiation therapy: a critical review on current status of clinical and preclinical studies and knowledge gaps. *Phys. Med. Biol.* **2024**, 69(10), 10TR02. <https://doi.org/10.1088/1361-6560/ad4192>.
  5. Sotiropoulos M.; Brisebard E.; Le Dudal M.; Jouvion G.; Juchaux M.; Crépin D.; Sebric C.; Jourdain L.; Labiod D.; Lamirault C.; Pouzoulet F.; Prezado Y. X-rays minibeam radiation therapy at a conventional irradiator: Pilot evaluation in F98-glioma bearing rats and dose calculations in a human phantom. *Clin. Transl. Radiat. Oncol.* **2021**, 27, 44–49. <https://doi.org/10.1016/j.ctro.2021.01.001>.
  6. McGarrigle J.M.; Long K.R.; Prezado Y. On the significance of the different geometrical and dosimetric parameters in microbeam and minibeam radiation therapy: A retrospective evaluation. *Front. Oncol.* **2024**, 1449293. <https://doi.org/10.3389/fonc.2024.1449293>.
  7. Prezado Y.; Thengumpallil S.; Renier M.; Bravin A. X-ray energy optimization in minibeam radiation therapy. *Med. Phys.* **2009**, 36(11), 4897–4902. <https://doi.org/10.1118/1.3232000>.
  8. Fernandez-Palomo C.; Chang S.; Prezado Y. Should Peak Dose Be Used to Prescribe Spatially Fractionated Radiation Therapy?—A Review of Preclinical Studies. *Cancers* **2022**, 14(15), 3625. <https://doi.org/10.3390/cancers14153625>.
  9. Garcia D.A.; Fazzari J.M.; Hlushchuk R.; Khoma O.Z.; Bakken K.K.; Burgenske D.M.; Lester S.C.; Mutter R.W.; Lucien F.; Remmes N.B.; Sarkaria J.N.; Park S.S.; Djonov V.G.; Grams M.P. Minibeam radiation therapy valley dose determines tolerance to acute and late effects in the mouse oral cavity. *Int. J. Radiat. Oncol. Biol. Phys.* **2025**, 1–8. <https://doi.org/10.1016/j.ijrobp.2025.03.016>.
  10. Prezado Y.; Lamirault C.; Larcher T.; Gilbert C.; Espenon J.; Patriarca A.; de Marzi L.; Corvino A.; Ortiz R.; Juchaux M. On the significance of peak dose in normal tissue toxicity in spatially fractionated radiotherapy: The case of proton minibeam radiation therapy. *Radiother. Oncol.* **2025**, 205, 110769. <https://doi.org/10.1016/j.radonc.2025.110769>.
  11. Bazyar S.; Inscoe C.R.; O'Brian E.T.; Zhou O.; Lee Y.Z. Minibeam radiotherapy with small animal irradiators: in vitro and in vivo feasibility studies. *Med. Phys.* **2020**, 47(10), 4879–4887. <https://doi.org/10.1002/mp.14406>.
  12. Grams M.P.; Quintero Mateus C.; Mashayekhi M.; Minibeam Radiation Therapy Treatment (MBRT): Commissioning and First Clinical Implementation. *Int. J. Radiat. Oncol. Biol. Phys.* **2024**, 120(5):1423–1434. doi:10.1016/j.ijrobp.2024.06.035.
  13. Herchko S.; Yaddanapudi S.; Wang C.K.C. Design and validation of a minibeam treatment delivery system for use with a radiation therapy research platform [Accepted manuscript]. *Biomedical Physics & Engineering Express*. **2025**, <https://doi.org/10.1088/2057-1976/adcf2c>.
  14. Babcock K.; Sidhu N.; Kundapur V.; Ali K. Collimator design for experimental minibeam radiation therapy. *Med. Phys.* **2011**, 38(4):2192–7. <https://doi.org/10.1118/1.3560>.
  15. Mettievier G.; Luongo N.; Crimaldi U.; Pacelli R.; Clemente S.; Oliviero C.; Lai Y.; Jia X.; Cerbone L.A.; Fiorino C.; Spinelli A.; Russo P. VIT-MBRT, a GPU-based virtual imaging platform dedicated to minibeam radiation therapy for preclinical research. In Bakic, P. et al., *Proceedings Virtual Imaging Trials in Medicine* **2025**, pag. 36. <https://doi.org/10.5281/zenodo.16754124>
  16. Buffardi E.; Cerbone L.A.; Crimaldi U.; Franciosini G.; Schiavi A.; Patera V.; Russo P.; Mettievier G. FREDem: a multi GPU Monte Carlo simulation code for virtual imaging trials in radiology. In Bakic, P. et al., *Proceedings Virtual Imaging Trials in Medicine* **2025**, pag. 170. <https://doi.org/10.5281/zenodo.16754124>
  17. Koksak Akbas C.; Vurro F.; Fiorino C.; Cozzarini C.; Cavaliere F.; Milani P.; Broggi S.; Del Vecchio A.; Di Muzio N.; Tacchetti C.; Spinelli A. Preclinical photon minibeam radiotherapy using a custom collimator:

- Dosimetry characterization and preliminary in-vivo results on a glioma model. *Physica Medica* **2024**, *124*:103420.
18. Poludniowski G.; Landry G.; DeBlois F.; Evans P.M.; Verhaegen F. SpekCalc: a program to calculate photon spectra from tungsten anode x-ray tubes. *Phys Med Biol* **2009**, *54*(19):N433-N8.
  19. Poludniowski G.G. Calculation of x-ray spectra emerging from an x-ray tube. Part II. X-ray production and filtration in x-ray targets. *Med. Phys.* **2007**, *34*(6):2175-86.
  20. Faddegon B.; Ramos-Méndez J.; Schümann J.; McNamara A.; Shin J.; Perl J.; Paganetti H. The TOPAS Tool for Particle Simulation, a Monte Carlo Simulation Tool for Physics, Biology and Clinical Research. *Phys. Med.* **2020**, *72*:114-121.
  21. Pellicoli P.; Donzelli M.; Davis J.A.; Estève F.; Hugtenburg R.; Guatelli S.; Petasecca M.; Lerch M.L.F.; Bräuer-Krisch E.; Krisch M. Study of the X-ray radiation interaction with a multislit collimator for the creation of microbeams in radiation therapy. *J. Synchrotron Radiat.* **2021**, *28*(2), 392–403. <https://doi.org/10.1107/S1600577520016811>.
  22. Ahmed M.; Beyreuther E.; Gantz S.; Horst F.; Meyer J.; Pawelke J.; Schmid T.E.; Stolz J.; Wilkens J.J.; Bartzsch S. Design and dosimetric characterization of a transportable proton minibeam collimation system. *Front. Oncol.* **2024**, *14*, 1473625. <https://doi.org/10.3389/fonc.2024.1473625>

**Disclaimer/Publisher's Note:** The statements, opinions and data contained in all publications are solely those of the individual author(s) and contributor(s) and not of MDPI and/or the editor(s). MDPI and/or the editor(s) disclaim responsibility for any injury to people or property resulting from any ideas, methods, instructions or products referred to in the content.